Heliyon 10 (2024) e41075

Contents lists available at ScienceDirect

Heliyon

journal homepage: www.cell.com/heliyon

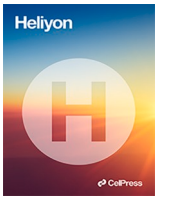

Research article

Electropolymerization of PPy, PEDOT, and PANi on WO_3 nanostructures for high-performance anodes in Li-ion batteries

Gemma Roselló-Márquez, Dionisio Miguel García-García, Mireia Cifre-Herrando, José García-Antón *

Ingeniería Electroquímica y Corrosión, Instituto Unversitario de Seguridad Industrial, Radiofísica y Medioambiental, Universitat Politècnica de València, C/Camino de Vera s/n, 46022, Valencia, Spain

ARTICLE INFO

Keywords:
WO_3 nanostructures
Polymer coatings
Li-ion batteries
Electrochemical behavior
Capacity

ABSTRACT

In this research work, four distinct WO_3 electrodes were synthesized and coated with three different polymers, known as polypyrrole (PPy), poly(3,4-ethylenedioxythiophene) in poly(4-styrenesulfonate) (PEDOT:PSS) and polyaniline (PANi), using electropolymerization techniques. The morphological features of the samples were thoroughly characterized through Field Emission Scanning Electron Microscopy (FE-SEM) and Atomic Force Microscopy (AFM) analyses. Additionally, contact angle measurements and electrochemical characterizations were used to verify the performance of each electrode, aiding in the prediction of their suitability for energy storage applications in lithium-ion batteries. The electrodes were subsequently employed as anodes in lithium-ion batteries, and charge-discharge cycles were performed to analyze its specific capacity, and the Electrochemical Impedance Spectroscopy (EIS) technique was employed to analyze its behavior both before and after cycling. The results revealed superior performance for WO_3 electrodes with PEDOT:PSS coating electropolymerized during 100 min at 0.4 mA. This comprehensive investigation not only sheds light on the synthesis and morphological characteristics of WO_3 electrodes but also highlights the crucial role of PEDOT:PSS in enhancing electrochemical behavior for efficient energy storage applications.

1. Introduction

In recent years, there has been a growing focus on the development of innovative hybrid materials, which integrate organic and inorganic compounds. One particularly prominent area of research involves the utilization of conducting polymers as conductive matrices, combined with transition metal oxides. This promising path of investigation will be able to provide a wide range of novel functional materials, demonstrating remarkable potential across various applications, including electrochromic materials, energy storage solutions, and photocatalysts [1].

Among the various inorganic materials explored in this context, tungsten oxide has emerged as a studied candidate, primarily for its role as a negative electrode and as an energy storage material. Tungsten oxide, known as WO_3, exhibits excellent chemical stability and a strong affinity for substrate adherence [2].

Remarkably, WO_3 can exist in various crystallographic structures, featuring 3-D networks of WO_6 octahedra organized in corner-sharing or edge-sharing configurations. This structural versatility offers numerous channels and chains of interstitial sites ideal for the

* Corresponding author.
E-mail address: jgarciaa@iqn.upv.es (J. García-Antón).

https://doi.org/10.1016/j.heliyon.2024.e41075
Received 9 July 2024; Received in revised form 3 December 2024; Accepted 6 December 2024
Available online 10 December 2024

insertion of small ions, which serve as the foundation for the material's electrochemical behavior [3].

The kinetics of redox processes in tungsten oxides are significantly influenced by their structural variations and, consequently, the synthesis methodologies employed. In many examples, the redox reactivity of WO_3 is hindered by the sluggish diffusion within compact tungsten oxide structures [4]. To address this challenge, intrinsically conducting polymers have recently been employed as matrices to incorporate WO_3 particles, facilitating the efficient transport of charge to the oxide.

Particularly remarkable is the incorporation of WO_3 nanostructures into polymers such as polyaniline (PANI), polypyrrole (PPy), and poly(3,4-ethylenedioxythiophene) (PEDOT), resulting in composite materials. This method has produced impressive results, such as expediting redox processes within the WO_3 component by improving charge transport beyond the polymer layer to the metal oxide. Moreover, the elevated surface-to-volume ratio in these composite structures additionally aids ion transport [5]. The production of nanostructured WO_3/conducting polymer composites synergistically boosts their pseudo-capacitive properties, capitalizing on the advantages offered by both constituent materials [6].

Furthermore, it is of interest to investigate whether these interactions can lead to the emergence of entirely new properties within the composite. Alternatively, it is conceivable that the composite merely gets the properties of its original components, exhibiting additive performance. This suggests that the electronic structure and properties of the individual components are faithfully retained within the composite. Exploring these aspects of composite materials holds great promise for advancing our understanding and optimizing their applications [7].

Polypyrrole (PPy) stands out as a polymer renowned for its exceptional attributes. These include its remarkable stability in the oxidized state, favorable redox characteristics, impressive electrical and optical properties, and its ability to be synthesized through straightforward electrochemical methods. Given these qualities, PPy and its derivatives find extensive application in electrochemical capacitors. They are valued for their rapid and reversible insertion/de-insertion capacity, high conductivity, robust thermal and environmental stability, and efficient storage capability [8,9].

On the other hand, Polyaniline is an excellent conductive polymer that can be polymerized with aniline monomers through various techniques, offering advantages due to its easy preparation, acid/base chemistry (insertion/de-insertion), and environmental stability [9].

Finally, PEDOT is one of the most important and effective conductive polymers synthesized in the field of organic electrochemistry. It exhibits great hole mobility (17.4 $cm^2 V^{-1} s^{-1}$), high conductivity (882 S cm^{-1}) and allows for easy modification of its properties. All these characteristics make PEDOT a suitable and important material for a wide choice of applications, such as photovoltaic cells, fuel cells, sensors, and supercapacitors. Moreover, Poly(4-styrenesulfonate) (PSS^-) is commonly incorporated into PEDOT through chemical or electrochemical methods. When PEDOT undergoes oxidation, the positively charged units on its backbone engage with the sulfonate groups of PSS^-. Conversely, upon reduction of PEDOT, these sulfonate groups interact with other cations in the solution to ensure charge neutrality within the film. Due to steric hindrance, PSS^- faces difficulty leaving the blend structure, resulting in cation exchange in PEDOT:PSS [10].

Therefore, this study is focused on the improvement of the electrochemical behavior of WO_3 nanostructures as anode in lithium-ion batteries coated with the polymers mentioned above. For this purpose, the applied cycles and the electrolyte used will be varied in coatings synthesized by cyclic voltammetry (CV) (such as PPy and PANi). On the other hand, the time and intensity applied will be changed in the case of the coatings synthesized by the galvanostatic mode (PEDOT:PSS). Once synthesized, they will be morphologically and structurally characterized by FE-SEM, XRD, contact angle and AFM. In addition, they will be electrochemically characterized, and the electrochemically active area will be determined. Finally, the behavior as anode in lithium-ion batteries will be assessed by means of charge and discharge curves and their analysis by EIS both before and after applying 30 cycles to study their useful life.

2. Experimental method

2.1. Synthesis of WO_3 nanostructures

Electrochemical anodization was employed to synthesize nanostructures of tungsten oxide. Tungsten foil with a purity of 99.5 % was got from Sigma Aldrich and subsequently cut into 2 cm × 2 cm samples. These samples underwent a cleaning process before being dipped in a solution of ethanol (100 mL) and subjected to sonication within a reaction flask. The anodization process was conducted utilizing a system comprising an anode (the tungsten foil sample) and a cathode (platinum), with a voltage of 20 V applied for 4 h while maintaining the electrolyte temperature at a constant 50 °C. The electrolyte used during electrochemical anodization was 1.5 M methanesulfonic acid (CH_4O_3S) and 0.05 M H_2O_2. Following anodization, the samples were subjected to annealing for a duration of 4 h in an air environment at 600 °C [11].

2.2. Electropolimerization of PPy, PEDOT and PANi

The nanoporous WO_3 served as the working electrode, while a reference electrode made of Ag/AgCl (3 M KCl) and a counter electrode featuring a platinum (Pt) tip were employed. All experimental procedures were conducted under standard environment at room temperature (25 ± 2 °C).

2.2.1. PPy

The PPy shell was crafted using the electrochemical polymerization technique facilitated by a BioLogic electrochemical

workstation. Within this setup, the WO_3 sample, possessing an effective area of 2.5 cm^2, functioned as the working electrode within a 100 mL solution containing 0.1 M pyrrole and 25 mM of various supporting salts (sodium dodecyl sulfate (SDS), potassium chloride (KCl), and oxalic acid). Subsequently, deposition occurred within the potential range from −0.4 V to 1.0 V utilizing a potential dynamic method, with the applied cycles varying between 10 and 40 cycles [12].

2.2.2. PEDOT/PSS

Poly(3,4-ethylenedioxythiophene) (PEDOT) was synthesized via aqueous electropolymerization utilizing 0.01 M EDOT as the monomer and 0.1 M PSSNa as the supporting electrolyte. The growth process occurred within a three-electrode system, employing WO_3 nanostructures as the working electrode, platinum wire as the counter electrode, and Ag/AgCl (3 M KCl) electrode as the reference electrode. The electrochemical polymerization was carried out for durations of 25 and 100 min at current densities of 0.4 and 1 mA, respectively, resulting in the formation of WO_3/PEDOT core-shell nanorod arrays [7].

2.2.3. PANi

To deposit polyaniline (PANI), a polymerization solution containing 0.2 M aniline monomer and 0.5 M aqueous sulfuric acid was utilized. Subsequently, electrodeposition was carried out within the potential range from −0.2 V to 1.0 V using a potential dynamic method with 5, 10, and 20 cycles conducted at room temperature [6].

2.2.4. Impedance spectra

During electropolymerization, EIS was performed every few cycles in the case of PPy and PANi and every few minutes in the case of PEDOT:PSS in order to monitor the electrochemical behavior of the polymer layer being deposited and to be able to analyze a first approximation of the performance of each case.

The common conditions under which the EIS were performed were at a potential of 1 V (with a 10 mV amplitude) and a scanning frequency ranging from 10 KHz to 10 mHz. However, the particular conditions were as follows: In the case of PPy, the EIS tests were performed every 5 cycles (from 0 to 40 cycles) in the electrolyte in which the electropolymerization was performed (0.1 M pyrrole and 25 mM of various supporting salts (sodium dodecyl sulfate (SDS), potassium chloride (KCl), and oxalic acid)) using a standard three-electrode cell setup. In the case of PEDOT:PSS, every 25 min (between 0 min until 125 min) were performed at different current densities in an electrolyte of 0.01 M EDOT as the monomer and 0.1 M PSSNa as the supporting electrolyte. In the case of PANi the EIS measurements were performed every 5 cycles from 0 cycles to 20 and in an electrolyte of 0.2 M aniline monomer and 0.5 M aqueous sulfuric acid in the same setup.

2.3. Contact angle

The contact angle between a water droplet and the film surface was determined using a Contact Angle Meter–KRUSS DSA100 equipment. The hydrophilicity or hydrophobicity of the electropolymerized films was assessed by determining the contact angle of water droplets placed on the film surface. Contact angle tests were conducted using 2 μL water at three different positions per film, twice in each electrode.

2.4. Morphology and structural characterization

The morphology of the prepared samples was analyzed using FE-SEM with a Zeiss Ultra 55 microscope operated at 3 kV. X-ray diffraction analysis was performed using a Rigaku D/MAX2500V instrument with Cu Kα radiation ($\lambda = 0.15418$ nm). Three-dimensional Atomic Force Microscopy (AFM) images of the composite were acquired to investigate surface roughness using a SPA-300 HV instrument. AFM measurements were conducted in intermittent contact-mode (ic mode) using a VeccoCP Research microscope equipped with a silicon tip with a diameter of 20 nm and a 22° apex angle. The electronic structure and chemical state of the elements in the samples were examined using X-ray photoelectron spectroscopy (XPS). Composition data were acquired with the K-ALPHA system from Thermo Scientific, utilizing Al-Kα radiation (1486.6 eV). The pass energy was set to 50 eV, and the pressure was maintained at 10ˆ-7 Torr."

2.5. Electrochemical characterization

2.5.1. EIS and capacitance measurements before application

The EIS experiments were carried out using a standard three-electrode cell setup, consisting of a WO_3 electrode coated with various polymer deposits as the working electrode, a platinum tip as the counter electrode, and an Ag/AgCl (3 M KCl) electrode acting as the reference electrode. EIS measurements were conducted in a 0.1 M H_2SO_4 aqueous solution at a potential of 1 V (with a 10 mV amplitude) and a scanning frequency ranging from 10 KHz to 10 mHz.

The specific capacitance (Cdl) of different active materials was determined using a standard three-electrode electrochemical cell setup. A polymer/WO_3 electrode is used as the working electrode, with a 3 M Ag/AgCl reference electrode and a platinum wire as the counter electrode. The electrolyte consists of 0.5 M H_2SO_4 solution, and the system is purged with argon to ensure an inert atmosphere. The cell is maintained at 25 °C during measurements.

The Cdl, which is determined using scan rate-dependent cyclic voltammetry. The procedure involves performing cyclic voltammetry over a potential range that excludes faradaic processes, ensuring that only capacitive charging is measured. Potential cycling

was performed from 0 to 0.4 V for four cycles at scan rates of 10, 20, 50, 100, and 200 mV·s−1 with automatic iR compensation. The capacitive current is plotted against the scan rate, and the slope of this plot gives the Cdl.

The current at 0.2 V for both the anodic and cathodic sweeps of the last cycle was extracted, and the differential capacitance of the cells was calculated using Equation (1):

$$i = EDLC \cdot \frac{dV}{dt} \quad \text{(eq. 1)}$$

In the equation, i represents the average absolute current (in mA) at 0.2 V (vs Ag/AgCl), EDLC denotes the electric double-layer capacitance (in F), and dV/dt stands for the scan rate (in $mV{\cdot}s^{-1}$).

Therefore, the estimation of the Electrochemically Active Surface Area (ECSA) of the materials can subsequently be computed using Equation (2) [13]:

$$ECSA = \frac{C_{dl}}{C_{Spec}} \quad \text{Eq 2}$$

where ECSA is electrochemical surface area (m^2), C_{dl} has been calculated from the cyclic voltammetries and C_{spec} is the area-specific capacitance of based material taken as 899 μF cm^{-2}.

2.5.2. GCD and EIS in Li-ion batteries

To evaluate the efficacy of different electrodes as anodes in lithium-ion batteries, both galvanostatic charging/discharging curves (GCD) and Electrochemical Impedance Spectroscopy (EIS) will be conducted. The batteries were assembled utilizing WO_3 nanostructure layers as the working electrode and lithium sheet as the counter electrode. The electrolyte solution (Merck) contained 1 M $LiPF_6$ dissolved in a nonaqueous mixture of dimethyl carbonate and ethylene carbonate, with a volume ratio of 1:1, and fiberglass spacers were employed. Battery assembly took place within a glove box under an inert atmosphere (argon), with each battery containing 300 μl of electrolyte volume.

Galvanostatic charge/discharge tests were performed with an Autolab PGSTAT302N potentiostat. Charging and discharging tests were conducted within a potential range from 0.01 V to 4 V versus Li/Li^+ at a current density of 100 mA g^{-1} [14]. The Electrochemical Impedance Spectroscopy (EIS) was examined at open circuit potential (OCP). Measurements were carried out over a frequency spectrum spanning from 10^5 to 0.01 Hz, employing an alternating sinusoidal signal of 5 mV. The equivalent circuit was simulated using the ZView software.

3. Results

3.1. Polymerizations

Fig. 1 displays the deposition curves of PPy thin films on WO_3 nanostructures, acquired via cyclic voltammetry (CV) mode.

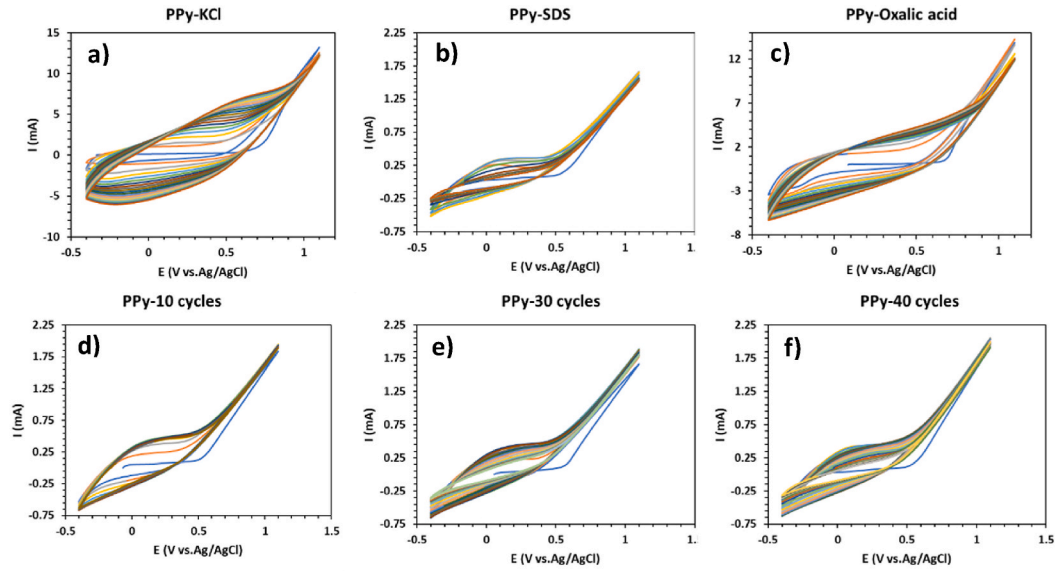

Fig. 1. Cyclic voltammograms of deposition of PPy at scan rate of 20 mV s^{-1} from a solution containing 0.1 M Pyrrol and a) 25 mM KCl during 20 cycles, b) 25 mM SDS during 20 cycles, c) 25 mM oxalic acid during 20 cycles, d) 25 mM SDS during 10 cycles, e) 25 mM SDS during 30 cycles and f) 25 mM SDS during 40 cycles on WO_3 nanostructures.

Analyzing the shape of these deposition curves enables elucidation of the nucleation and growth mechanisms of PPy thin films. As voltage is scanned, various redox reactions of the electroactive species in the solution take place at the electrode surface. A notable increase in current density typically occurs at +0.7 V (vs Ag/AgCl), indicating the oxidation of pyrrole (Py) monomers into radical cations and subsequent formation of PPy film on the WO_3 electrode, ensuring uniform coverage [15].

In Fig. 2, the cyclic voltammogram (CV) diagrams illustrating PANI deposition are presented. These diagrams were generated with a scan rate of 20 mV s^{-1} within a potential range spanning from −0.2 V to 1.1 V (vs Ag/AgCl) under the potentiodynamic mode. At −0.2 V, PANI undergoes complete reduction into the leucoemeraldine (LE) form, as depicted in Fig. S1, resulting in the formation of a thin yellow film. During the first oxidation process at 0.45 V, the reduced state does not entirely oxidize, leading to the emerald state (EM) (Fig. S1) and a green film. Upon reaching 1 V, the EM state undergoes complete oxidation to yield PANI, resulting in the formation of a blue-violet thin film [16].

In contrast to cyclic voltammetry (CV) mode, the galvanostatic (GS) mode entails applying a constant current while monitoring potential changes. Fig. 3 illustrates the deposition curve of PEDOT:PSS thin films under applied constant current densities of 0.4 and 1 mA. After the electrochemical double layer formation in each instance, the potential gradually declines, signaling the generation of oligomers on the electrode with a lower oxidation potential than the initial monomer. As depicted in Fig. 3, a higher initial potential is essential to initiate the oxidation of monomers into oligomers. Later, the constant potential achieved is sufficient for the complete polymerization process [17].

3.2. EIS during electropolymerization

In order to study the behavior during the electropolymerization in the three chosen polymers, impedances were carried out between cycles (every 5 cycles in the case of electropolymerizations using CV (PPy and PANi) and every 25 min in the case of the galvanostatic electropolymerizations (PEDOT:PSS). In Fig. 4, Nyquist diagrams are shown during the electropolymerization of PPy (Fig. 4a), PEDOT (Fig. 4b and c) and PANi (Fig. 4d).

In Fig. 4a, it is observed how the width of the semicircle associated with the charge transfer [18] decreases until the application of 30 cycles, and then this resistance begins to increase. With this result it can be predicted that after the application of 30 cycles, the coating will have less resistance to the charge transfer and therefore will present a better electrochemical behavior. This statement will be verified in subsequent characterizations.

In the case of PEDOT, it is observed that after reaching 100 min at both 0.4 mA and 1 mA the resistance presents a minimum value.

And finally, in the case of PANi the minimum resistance value is found after applying 10 cycles, therefore, with the next characterizations it will be confirmed which electropolymerization conditions are optimal.

3.3. Morphological and structural characterization

In order to analyze the nanoscale morphological characteristics of both the basic WO_3 and the coated electrodes, FE-SEM images were captured at a magnification of 20000. Fig. 5a displays the FE-SEM images of the uncoated oxide samples. It is evident that WO_3 exhibits a highly porous structure with a significant surface area, indicating effective etching of the tungsten surface by peroxide groups during electroanodization. Representative FE-SEM pictures for the hybrid samples are depicted in Fig. 5b–g, showcasing the deposition of PPy at 10, 20, 30, and 40 cycles in SDS as a supporting salt, as well as using KCl and oxalic acid as supporting salts. During the electrodeposition of PPy, the WO_3 globular structures were enveloped by a thin layer of nanometer-sized lamellar formations (ranging from 100 to 500 nm), causing cauliflower-like agglomerates. The morphology is similar in all cases, observing that as the cycles increase, there is a more uniform layer of PPy until reaching 30 cycles, beyond which the surface layer of the polymer presents uncovered gaps. Regarding the supporting salt, there is not much difference in the obtained morphology.

Fig. 5h–k showcase the morphological attributes of electrodeposited PEDOT:PSS nanofibers, which are characterized by their elongated, uniformly cylindrical shape, and random distribution. It can be observed that by carrying out electrodeposition for a longer period, a greater quantity of fibers is deposited. However, when applying less intensity, these fibers become finer, and therefore, the sample exhibits a larger surface area.

Finally, in Fig. 5l–n the morphology obtained from the samples electroplated with PANi is shown. Compared to the uncoated oxide

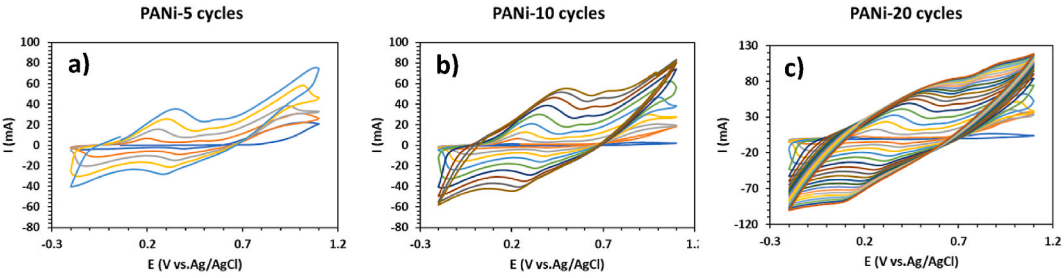

Fig. 2. Cyclic voltammograms of deposition of PANi at scan rate of 20 mV s^{-1} from a solution containing 0.2 M aniline and 0.5H_2SO_4 during a) 5 cycles, b) 10 cycles and c) during 20 cycles on WO_3 nanostructures.

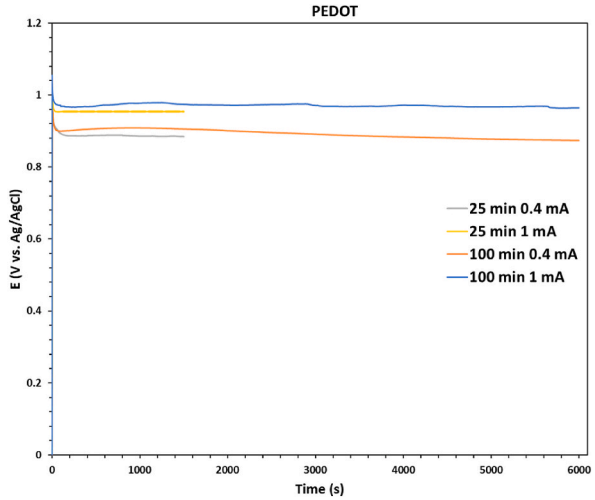

Fig. 3. Galvanostatic electropolymerization of PEDOT:PSS coatings on WO_3 nanostructures.

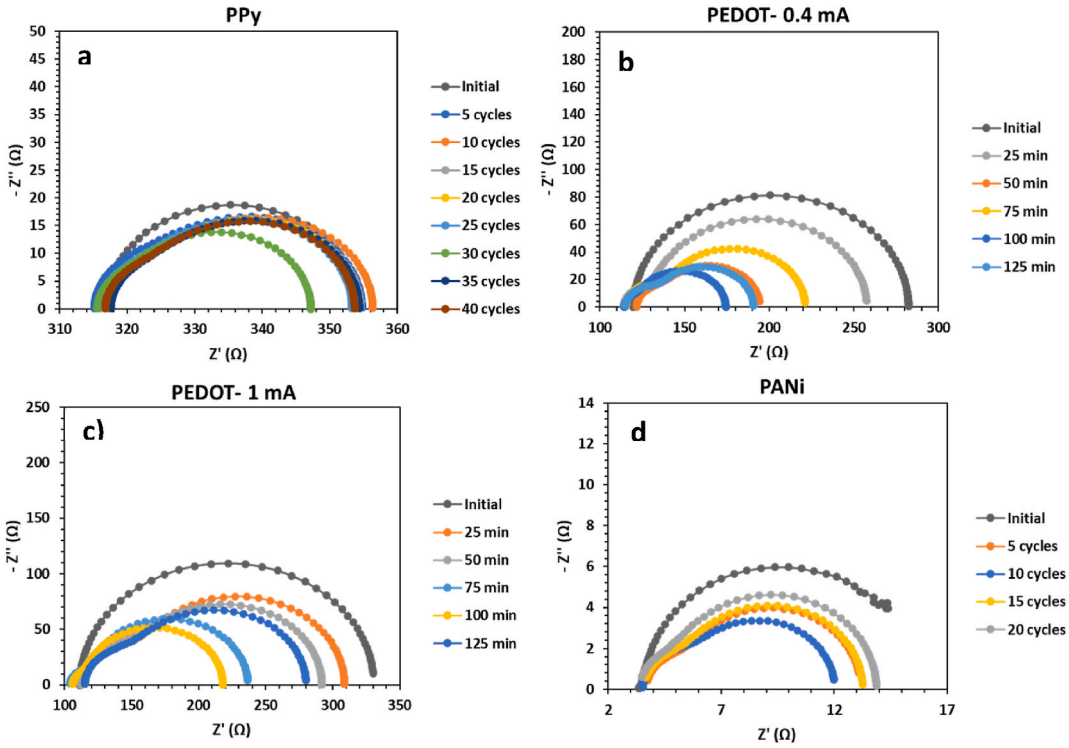

Fig. 4. EIS during electropolymerization of a) PPy, b) PEDOT at 0.4 mA, c) PEDOT at 1 mA and d) PANi.

support depicted in Fig. 5a, the most prominent differences are observed in the increase of grain size to resemble the bare WO_3, attributed to the homogeneous, skin-like coverage by the deposited polymer. Additionally, there is a noticeable decrease in the inter-grain spacing (pore size). After applying 20 cycles, it is observed that cracks begin to appear on the polymeric layer, which would compromise its stability and electrochemical properties.

In latter section we will further investigate the wettability of the samples according to surface roughness and morphologies obtained.

To study the crystallinity of the sample, Fig. 6 shows the X-ray diffraction (XRD) characteristic crystalline peaks of WO_3 across all samples, confirming that the tungsten trioxide phase remains present after the electropolymerization processes. The analysis involves three primary cases: WO_3 electropolymerized with polypyrrole (PPy), poly(3,4-ethylenedioxythiophene) (PEDOT), and polyaniline (PANi), each under various conditions.

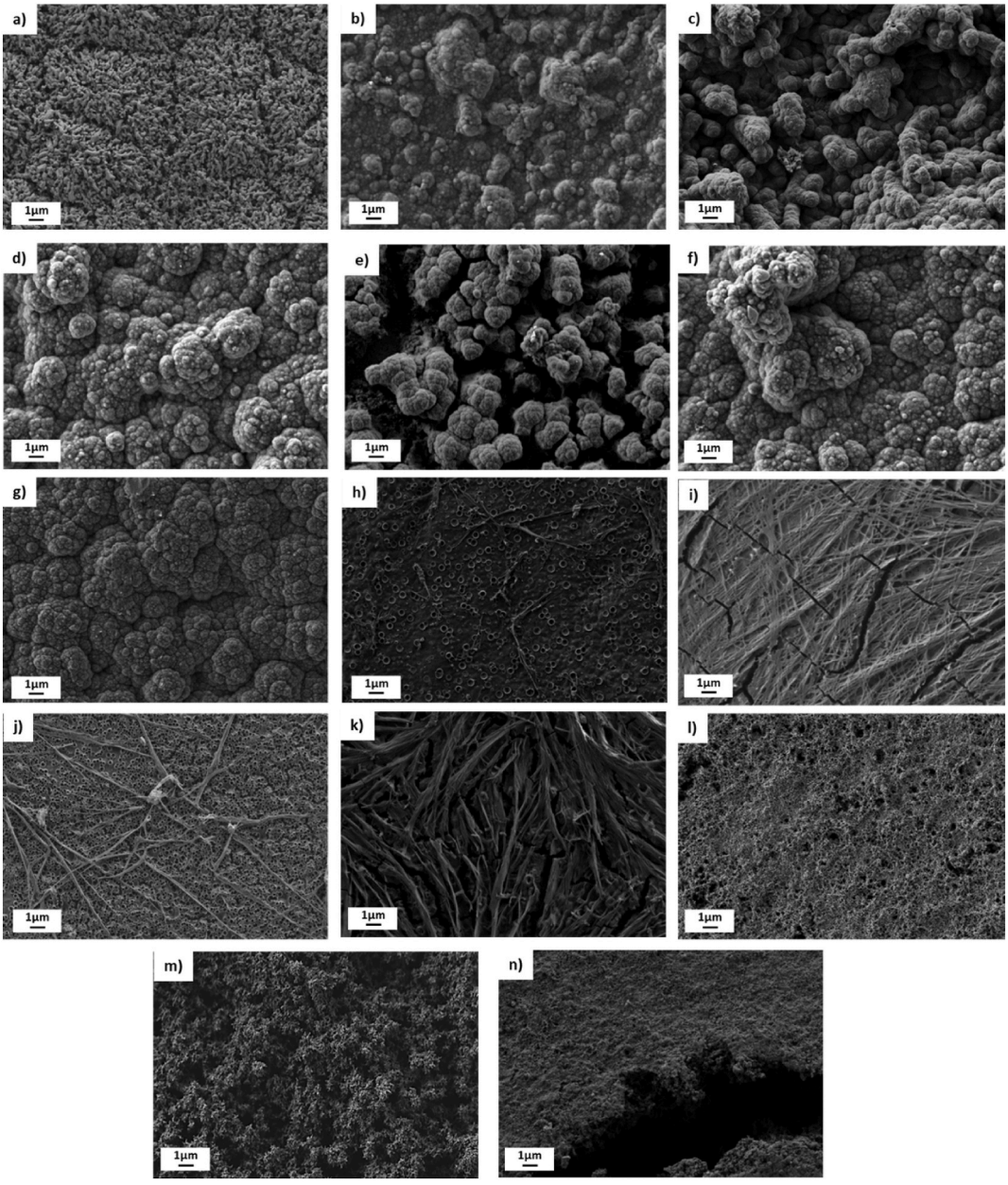

Fig. 5. FE-SEM images at 20000x of the surface of a) WO_3, b) PPy with SDS as supporting salt during 10 cycles, c) PPy with SDS as supporting salt during 20 cycles, d) PPy with SDS as supporting salt during 30 cycles, e) PPy with SDS as supporting salt during 40 cycles, f) PPy with oxalic acid as supporting salt during 20 cycles, g) PPy with KCl as supporting salt during 20 cycles, h) PEDOT during 25 min at 0.4 mA, i) PEDOT during 100 min at 0.4 mA, j) PEDOT during 25 min at 1 mA, k) PEDOT during 100 min at 1 mA, l) PANi during 5 cycles, m) PANi during 10 cycles and n) PANi during 20 cycles.

The characteristic peaks for the WO_3 phase are consistently observed across all samples, appearing prominently at 2θ angles of approximately 23.1°, 23.6°, and 24.4°, corresponding to the (002), (020), and (200) planes, respectively. These peaks confirm that the WO_3 maintains its crystalline structure after the electropolymerization process.

Regarding PPy electropolymerizations, the WO_3 peaks remain dominant. The inset highlights a smaller peak associated with PPy incorporation, appearing at around $2\theta \approx 24.6°$. This peak corresponds to the characteristic PPy reflection, indicating successful polymer integration. Among the variations, the sample with SDS as supporting salt in the electrolyte and electropolymerized during 30 cycles shows stronger peaks, suggesting optimal crystallinity and incorporation under these conditions.

In Fig. 6c, the results about PEDOT:PSS electropolymerization are shown. The characteristic WO_3 peaks remain intact, with two additional small peaks observed at $2\theta \approx 16.9°$ and 24.6°, corresponding to PEDOT incorporation. The sample with lower current

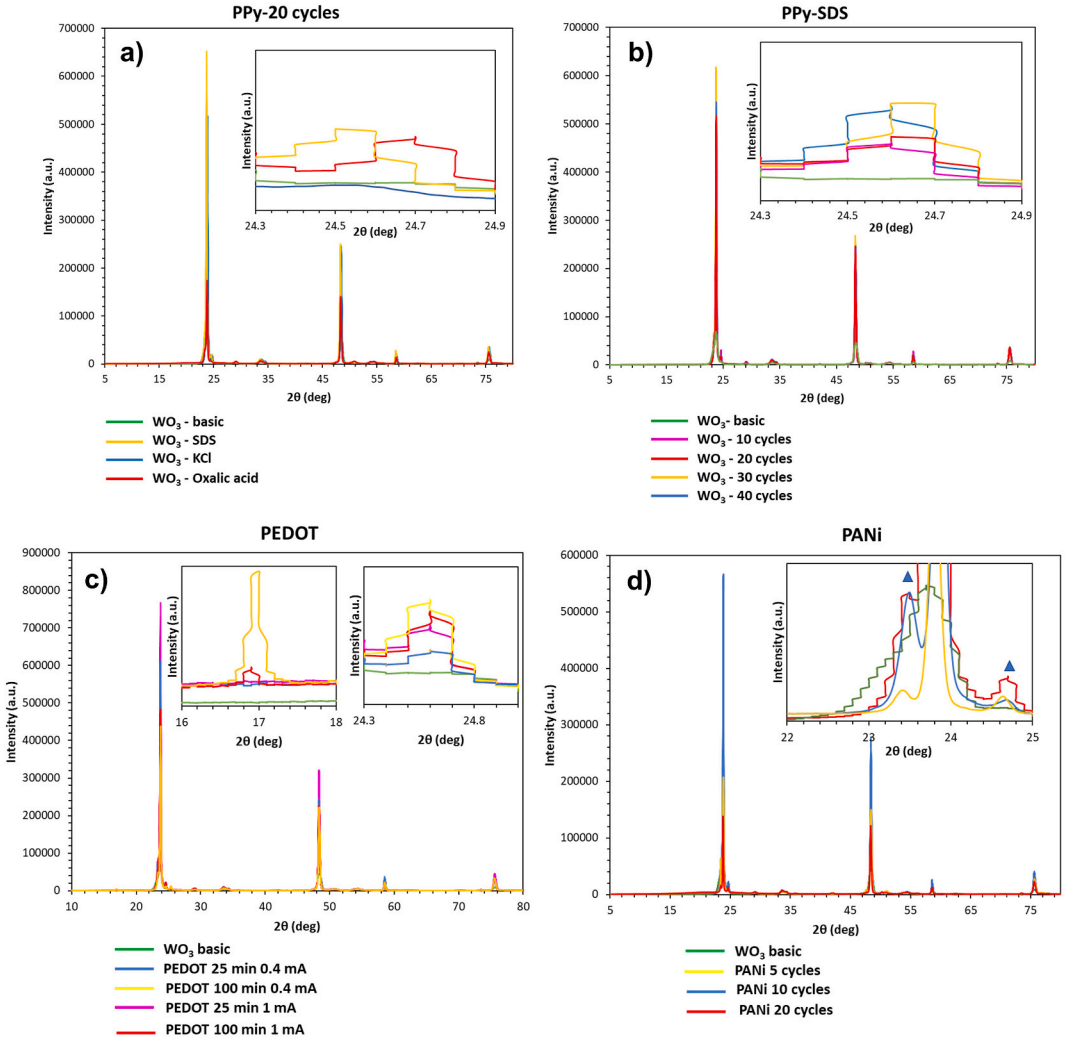

Fig. 6. XRD patterns of WO_3 nanostructures electropolymerized with a) and b) PPy, c) PEDOT:PSS and d) PANi at different conditions.

density and longer electropolymerization time exhibits more pronounced peaks, suggesting these conditions favor better PEDOT integration and enhanced crystallinity.

Finaly, in Fig. 6d, the XRD patterns reveal the usual WO_3 peaks, with two peaks indicating PANi presence at $2\theta \approx 23.5^{\circ}$ and 24.7°. The sample electropolymerized with 10 cycles shows the strongest peaks, suggesting better-defined crystal structures and more effective PANi incorporation.

In conclusion, the XRD patterns clearly indicate the crystalline structure of WO_3 is maintained in all samples, with the insets confirming the presence of the respective polymers at their characteristic 2θ angles.

X-ray Photoelectron Spectroscopy (XPS) was also performed to analyze the surface composition of the electrode, providing information on the chemical states of the elements and the atomic percentage of them in every sample. In Fig. S2 the XPS spectra of each electrode are shown while the atomic percentage is presented in in Table S1.

The C 1s peak near 284 eV reflects the presence of sp^2-hybridized carbon atoms in these aromatic systems. The carbon peaks are most prominent in the PPy, PEDOT:PSS and PANi samples, which is expected because these materials are carbon-based polymers. The WO_3 sample has a relatively small carbon peak, consistent with the fact that it is an inorganic oxide (tungsten trioxide), and carbon is not a major component. Any carbon present in WO_3 is likely from surface contamination, leading to a weaker peak.

The nitrogen peaks (N 1s peak) is shown around 399–400 eV. These peaks are most pronounced in the PPy and PANi samples, where nitrogen is an integral part of the polymer structures. The nitrogen atoms in PANi are part of its amine and imine groups, contributing to the stronger peak. The PPy nitrogen peak is also strong, which is expected due to the nitrogen present in the pyrrole rings. In WO_3 and PEDOT:PSS samples the nitrogen peaks much weaker indicating slight contamination or trace nitrogen incorporation.

The S 2p peak is typically split due to spin-orbit coupling into S 2p3/2 and S 2p1/2. The sulfur peaks are most prominent in the

PEDOT:PSS sample, which is expected because both PEDOT and PSS contain sulfur in thiophene rings of PEDOT and the sulfonate groups of PSS. PPy and PANi electrodes do not contain sulfur in the structure so both samples show weak sulfur peaks due to contamination during the synthesis process, while WO_3 barely shows any sulfur.

The Oxygen peaks (O 1s peak) are shown around 530 eV. They are prominent in all samples, but most intense in the WO_3 sample. WO_3 shows the most intense oxygen peaks, which is expected given its high oxygen content (67.2 %). The material is a metal oxide (WO_3), where oxygen atoms form a significant portion of the structure. PEDOT:PSS also shows noticeable oxygen peaks, consistent with its oxygen content (19.15 %) from the ethylenedioxy group in PEDOT and the sulfonate groups in PSS. Finally, PPy and PANi show weaker oxygen peaks, in line with their oxygen content (20.14 % and 15.55 %, respectively). In these samples, the oxygen content is due to surface oxidation or residual water/solvent molecules from the synthesis process and the detection of oxygen due to the WO3 nanostructures.

In the case of tungsten, W 4f doublet peaks are expected around 35–40 eV for tungsten oxides. The sample with the highest content is the WO3 electrode, since a quarter of the content is due to this element. In the rest of the samples, this element is barely detected, since its presence is only due to the WO3 nanostructures, but since XPS is a more superficial analysis, the detection of this element is

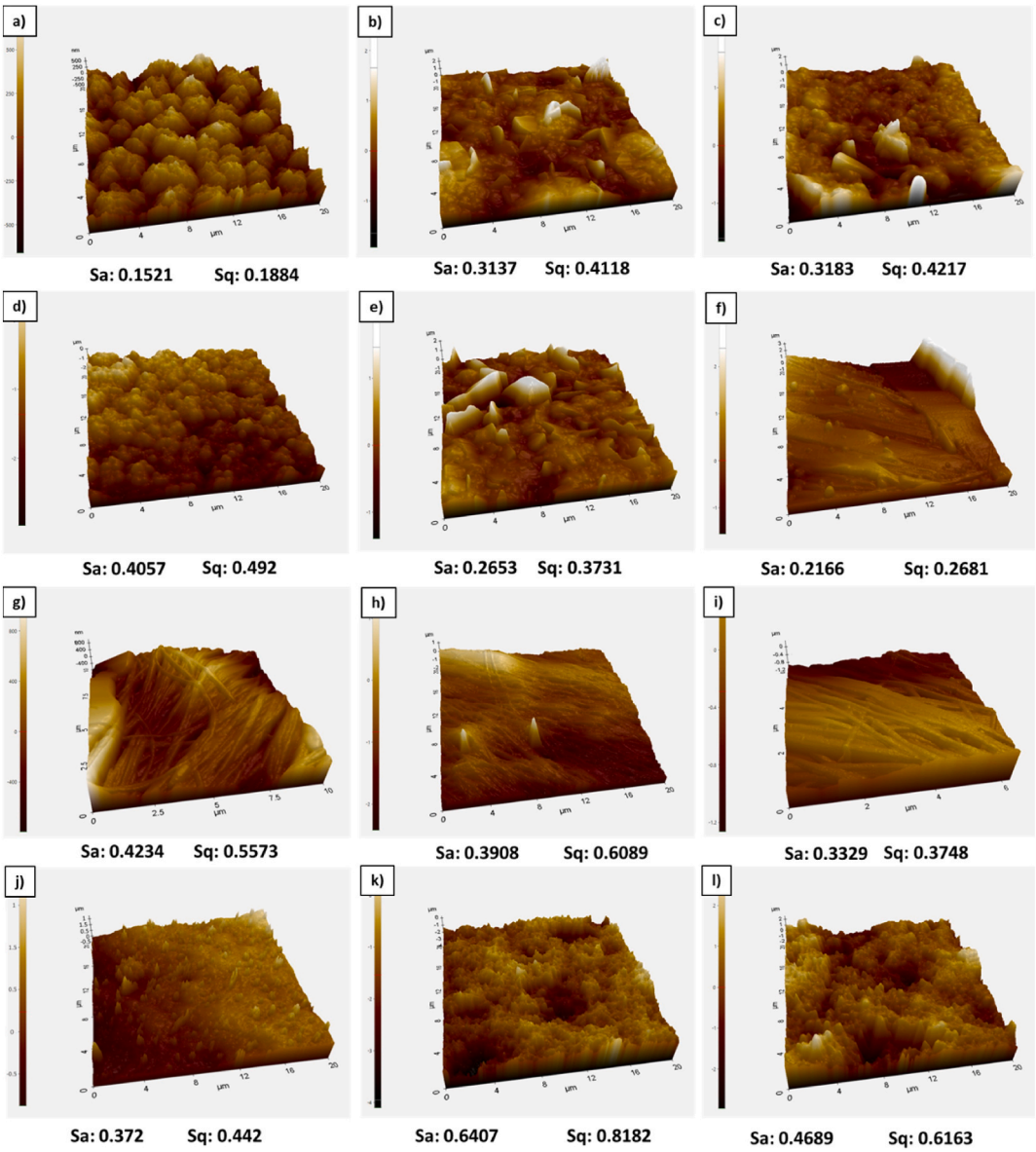

Fig. 7. 3D AFM images of a) WO_3, b) PPy with SDS as supporting salt during 10 cycles, c) PPy with SDS as supporting salt during 20 cycles, d) PPy with SDS as supporting salt during 30 cycles, e) PPy with SDS as supporting salt during 40 cycles, f) PEDOT during 25 min at 0.4 mA, g) PEDOT during 100 min at 0.4 mA, h) PEDOT during 25 min at 1 mA, i) PEDOT during 100 min at 1 mA, j) PANi during 5 cycles, k) PANi during 10 cycles and l) PANi during 20 cycles.

lower due to the deposition of polymers on top of the nanostructures.

Each sample aligns well with the expected chemical bonds and oxidation states, validating the material composition and surface characteristics.

To characterize the wettability of the electrodes, the contact angle technique has been employed In this technique, the angle formed by the water droplet that remains on the surface of the sample is analyzed, indicating whether it is a hydrophilic surface if the angle is less than 90°, or hydrophobic if it is greater than 90°. The results of the contact angle are shown in Fig. S3 and Table S2. As shown in Fig. S3a, the surface of bare WO_3 nanostructures is hydrophilic (contact angle 53.5°) but with the deposition of the different polymers this value change. On the one hand, the PPy film (Figs. S3b–f) shows cauliflower-like morphology with water contact angle between 60° and 96°, depending on the electropolymerization conditions employed. It can be observed that using SDS as a supporting salt, the observed contact angle is 84.23°, representing the lowest value observed concerning the electrolyte, exhibiting major hydrophilicity. Regarding the number of cycles, with 30 cycles, we obtain the sample with the highest hydrophilicity, resulting in a value of 60.63°. These intriguing findings suggest that the microstructures and wettability of the PPy films can be controlled by adjusting the cycle number during the electropolymerization process [19,20].

Regarding the samples synthesized with PEDOT:PSS (Figs. S3g-j), there are a clear difference between them. The values vary between 20° and 40°, being the sample obtained at 100 min and 0.4 mA which shows a lower contact angle (high hydrophilicity). This result can be clarified by considering that hydrophilic PSS has been deposited in greater quantity because the test has been carried out for a longer period [17,21,22]. However, when applying more intensity, the fibers are thicker, making the polymeric layer less hydrophilic than the layer with finer fibers and therefore, the contact angle is greater.

Finally, the contact angle of water on PANi samples (Figs. S3k–m) are the following: samples synthetized applying 5, 10 and 20 cycles present 80.8°, 45° and 99°, respectively. The improved wettability is maybe due to the sulfonation of aromatic rings during the electropolymerization reactions until applying 10 cycles. The water droplet entered into the composite, probably as a result of greater porosity, showing a contact angle lower than bare WO_3 electrode [23–25]. However, the sample obtained after 20 cycles shows highest water contact angle, being almost 100°.

In order to determine whether the polymeric layer affects the roughness of the basic WO_3 structure, the technique known as Atomic Force Microscopy (AFM) is used. In this study the area of 20 × 20 μm^2 of thin films sample were considered for topographic surface analysis. The room mean square roughness of the WO_3, PPy, PEDOT:PSS and PANi films obtained from the AFM analysis are shown in Fig. 7. AFM images of the WO_3 nanostructures show a smoother morphology compared with hybrid film. A rougher surface and hence a larger surface to volume ratio allows that the electrolyte ensure contact with all layers of the electrode, thereby enhancing its behavior as an anode in lithium-ion batteries compared with the relatively smooth surfaces [12,26]. The samples that exhibit higher roughness are those synthesized by applying 30 cycles with SDS as supporting salt in the case of PPy (Fig. 7b–e), those synthesized by applying 0.4 mA for 100 min in the case of PEDOT:PSS (Fig. 7f–i), and after applying 10 cycles in the case of PANi (Fig. 7j–l). In the case of PANi, it shows the highest roughness coefficient, so it would expect that this layer would exhibit the best wettability performance (it will be evaluated with the contact angle characterization) [27,28]. However, in the case of PEDOT:PSS, it serves as a conductive binder that links the WO_3 nanostructures, thereby reducing the electrical resistance of the resulting film. Additionally, the increased roughness of the nanowire, leading to the creation of valleys, can accumulate a greater number of electrolyte ions, thus enhancing the energy

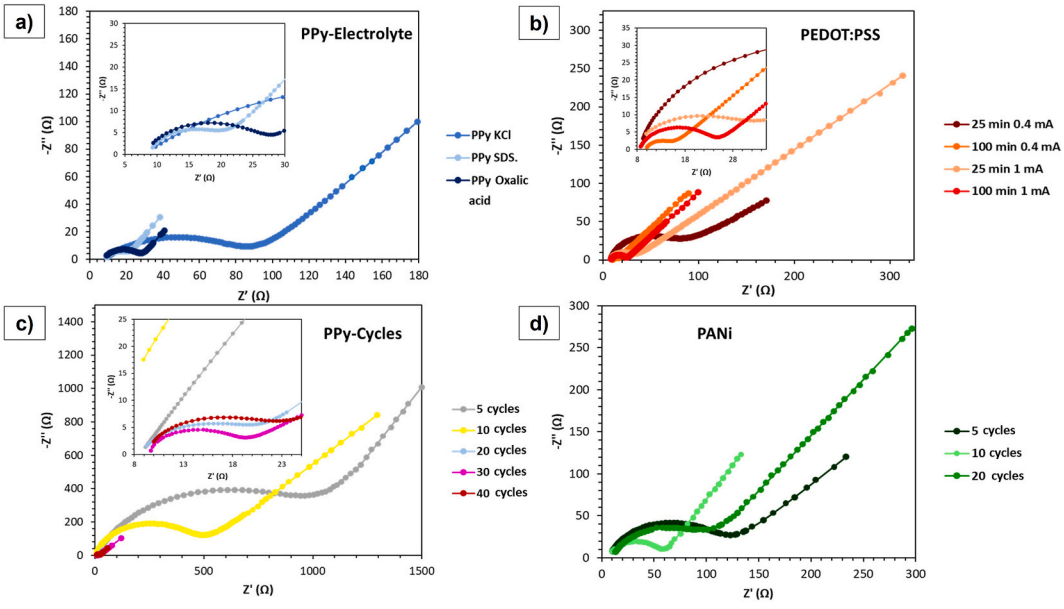

Fig. 8. Nyquist plot of a) PPy with different supporting salts during 20 cycles, b) PEDOT:PSS at different time and intensity, c) PPy with SDS as supporting salt during different cycles, d) PANi during different cycles.

storage capacity of the electrode [29–31].

3.4. Electrochemical characterization

Nyquist plots were employed to analyze the electrochemical impedance spectroscopy (EIS) data, with the equivalent circuit depicted in Fig. S4. Utilizing a three-electrode set up, the impedance of the electrode is assessed. Three distinctive features are observable across all cases. The initial tangent on the real axis (Z′) denotes the combined electrolyte resistance, representes as the sum of the ionic resistance (Rs) and the resistance introduced by the polymer layer (Rp) [32]. The electrode's conductivity is reflected by the Rct (charge transfer resistance) of the electrode material, which is represented by the radius of the semicircle in the low-to-high frequency region. Additionally, the third characteristic manifests as a sloping line at low frequencies [33,34]. This line corresponds to a Warburg element, indicating ion diffusion transport within the electrolyte. These measurements were taken at a 45-degree angle within the intermediate frequency range [35,36].

Therefore, after adjusting the data to the equivalent circuit shown in Fig. S4, the best results obtained by comparing the Rct values (Reduced values of the electrical resistive components indicate improved conductivity of the electrode.) according to the obtained coatings are as follows (Fig. 8): the electrode with a PPy layer exhibiting superior properties is synthesized after 30 cycles with SDS as the supporting salt (Fig. 8 c). In the case of PEDOT:PSS (Fig. 8b), the conditions that yield the best results, such as lower charge transfer resistance, are applying 100 min and 0.4 mA. Finally, after coating with PANi (Fig. 8d), the electrode with the best electrochemical characteristics was obtained after applying 10 cycles. All results are shown in Table 1.

To determine the electrochemically active area of each electrode, double layer capacitance (Cdl) tests were carried out by cyclic voltammetry measurements (Fig. S5). Fig. 9 presents the results of the C_{dl} values as well as the electrochemically active area of each electrode through cyclic voltammograms following the procedure explained in section 2.5.1 [37–39]. Measurements were conducted at different scan rates ranging from 10 to 200 mV s^{-1} within the positive potential range of 0–0.4 V vs. Ag/AgCl.

The voltammograms of each electrode suggest that the primary contribution to the measured net current comes from the charging of the double layer. Contributions from other electrochemical processes, such as redox reactions and adsorption/desorption processes, are found to be insignificant [13,40,41]. Notably, the area within the current curves expands as the scan rate increases, mirroring capacitive behavior (as depicted in Fig. S5).

After comparing the results obtained from all the synthesized electrodes, it can be concluded that the value of the double-layer capacitance, and therefore the value of the electrochemical surface area (ECSA), is higher in the case of the coating synthesized with PPy for 30 cycles and using SDS as the supporting salt (Fig. 9a and b). In the case of PEDOT (Fig. 9c), a larger electrochemically active area is obtained when the sample is synthesized for 100 min at 0.4 mA. Finally, in the case of the PANi polymer (Fig. 9 d), the one that yields the best results is obtained after applying 10 cycles of cyclic voltammetry (CV) (as it can be seen in Fig. 9).

In the end, comparing all the results, both morphological and electrochemical, it can be concluded that the electrode with the best properties for energy storage applications is the one obtained with PEDOT:PSS for 100 min at an intensity of 0.4 mA, having the greatest number of active sites due to a consequence of their alignment to the substrate [42,43]. However, these results obtained from all the previous characterizations will be compared with those obtained below after their use as anodes in lithium-ion batteries.

3.5. Energy storage application

3.5.1. Cyclic voltammetry tests

To check the electroactivity of the polymers a reactivation step has been included by subjective the electrodes to 3 cyclic voltammetry scans in the non-aqueous electrolyte before collecting any data, which allowed us to restore the electroactivity of the polymer films and stabilize their performance (Fig. S6).

Table 1
Rs + Rp and Rct values after analyzing and adjust the data to the equivalent circuit using ZView.

	Rs (Ω) + Rp (Ω)	Rct (Ω)
Basic WO_3	6.3	1290
PPy-KCl	13.3	89.6
PPy-SDS	13.2	12.2
PPy-oxalic acid	12.9	15.6
PPy- 5 cycles	12.9	1100
PPy- 10 cycles	12.1	459.5
PPy- 20 cycles	12.2	12.2
PPy- 30 cycles	11.5	8.5
PPy- 40 cycles	13.2	16.7
PEDOT-25 min 0.4 mA	10.6	60
PEDOT-100 min 0.4 mA	11.4	5.5
PEDOT-25 min 1 mA	11.35	21.2
PEDOT-100 min 1 mA	10.5	15.5
PANi-5 cycles	15.96	109.6
PANi-10 cycles	15.43	52.9
PANi-20 cycles	17.18	94.2

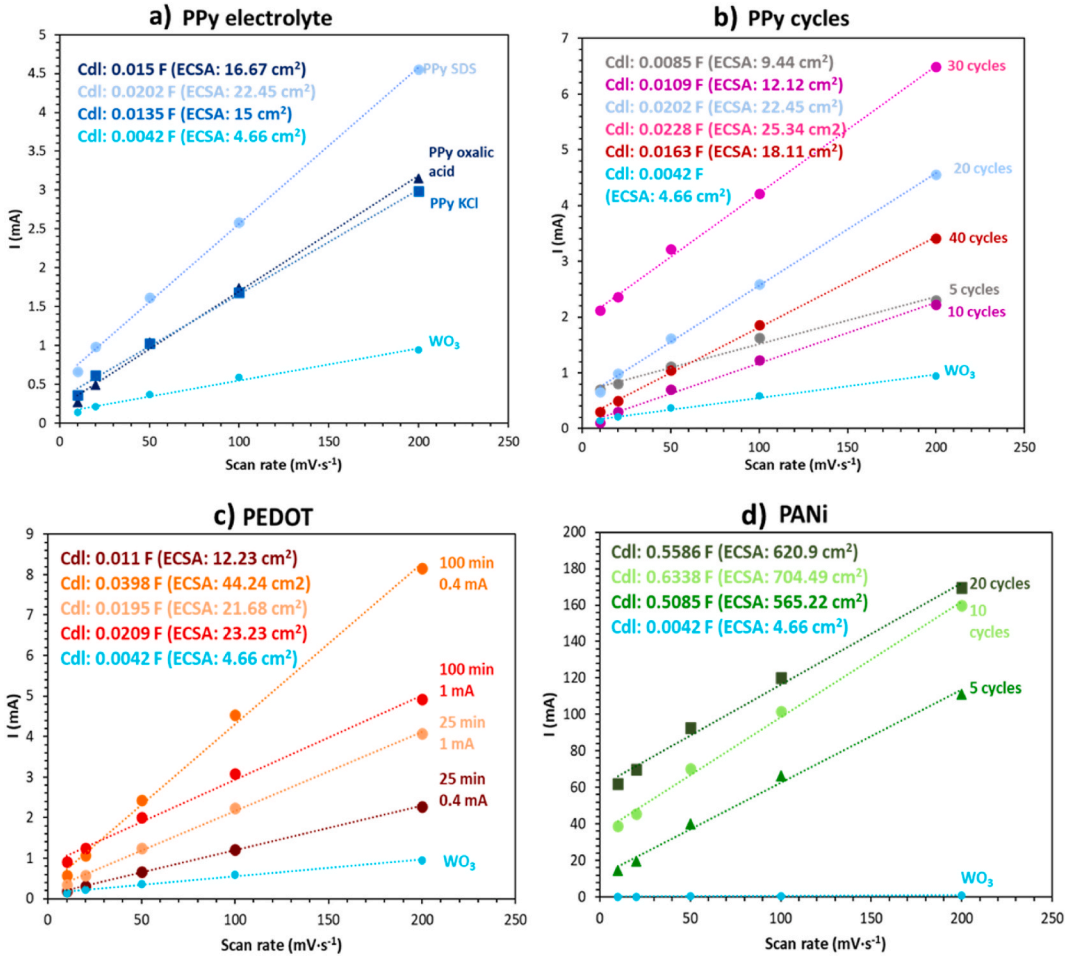

Fig. 9. Capacitance measurements of a) PPy with different supporting salts during 20 cycles, b) PPy with SDS as supporting salt during different cycles, c) PEDOT:PSS at different time and intensity and d) PANi during different cycles.

Across all samples, the first cycle shows a reduction peak related to SEI formation, appearing between 0.5 V and 0.7 V. This peak is associated with irreversible processes, where lithium is consumed to form the SEI layer. In subsequent cycles, the peaks shift to higher potentials (around 1.2 V–2.0 V), and the profiles of cycles 2 and 3 overlap significantly. This overlap indicates that the reactions occurring after the SEI formation are reversible and that the material reaches a stable state after the first cycle. These observations are crucial for understanding the electrochemical stability of the materials in lithium-ion batteries.

The reduction peak observed around 2.2 V during the first cycles likely corresponds to the reduction of a higher oxidation state species in the material. In the case of a polymer-based electrode material, the reduction peak at around 2.2 V could be related to the reduction of specific functional groups or redox-active sites within the polymer structure such as carbonyls (C=O), imines (C=N) during the lithiation process, where lithium ions are incorporated into the polymer matrix. This peak might represent the transition from a higher oxidation state to a lower one within the polymer backbone.

In case of WO3- base electrode this peak could be associated with the reduction of transition metal oxides or other electroactive species present in the electrode material, like tungsten.

In all cases the peak diminishes significantly in subsequent cycles, it could suggest that part of this reaction is not fully reversible or that structural changes in the material reduce the availability of electroactive sites. This behavior is crucial to understanding the electrochemical mechanisms and stability of the electrode materials during cycling."

3.5.2. Galvanostatic charge-discharge curves

The galvanostatic charge-discharge profile of all electrodes at 100 mA g^{-1} is presented in Fig. 10. The charge-discharge performance of every nanoelectrode shows three stages of voltage slide. The values of the potential of these three stages are different according to the electrode used. As can be observed, the electrodes that possess the polymeric layer show a higher initial potential value in the discharge curves (around 3.4 V), while the basic WO_3 electrode exhibits an initial potential value of 2.1 V when discharge potential is applied. However, this does not imply that electrodes with the electrodeposited polymer exhibit better performance as

anodes in batteries, as is not the case with PPy.

In all instances, the rapid discharge observed in the initial potential range is linked to the EDLC capacitance, while the subsequent voltage ranges indicate a combination of both pseudocapacitance and EDLC, characterized by longer discharge durations [3,44].

Furthermore, as depicted in Fig. 10, the presence of PANi, particularly PEDOT:PSS within the WO_3 matrix, reduces the electrode's internal resistance, facilitates charge transfer, and enhances specific capacitance storage. The delayed response noted in the final potential phase suggests an increased specific capacitance, especially evident in PEDOT:PSS, as electrolyte ions efficiently permeate to active inner sites, consequently enhancing electrode capacitance [45].

Hence, the enhanced behavior of the nanoelectrode is attributed to the effective movement of ions present in the electrolyte within the interconnected matrix of WO_3 and PEDOT:PSS during rapid charge-discharge cycles.

Furthermore, Fig. S7 shows the charge and discharge cycles of four different samples over the initial, 10th, 20th, and 30th cycles.

The WO_3-based electrode (Fig. S7a) shows a sharp voltage drop during the first discharge, characteristic of SEI formation. This indicates a significant initial capacity loss due to the formation of the SEI layer, which is common during the first cycle. The charge profile is relatively smooth, with a gradual voltage increase.

By the 10th cycle, there is a notable increase in the gap between the charge and discharge curves, indicating capacity fading. This suggests that the WO_3 electrode is experiencing significant degradation. The discharge curve has shifted, showing a reduced capacity compared to the first cycle.

In the last cycle, the WO_3 electrode continues to degrade. The charge and discharge profiles have moved further apart, and the overall capacity has decreased even more, reflecting substantial performance loss. This indicates that the WO_3 electrode is not maintaining stability over prolonged cycling.

The PPy-based electrode (Fig. S7b) also exhibits the expected SEI formation in the first discharge cycle. However, the voltage drop is slightly less pronounced compared to WO_3. The charging curve is smooth and follows a standard profile.

In the 30th cycle, the PPy electrode has lost more capacity than WO_3. The charge and discharge curves have diverged, reflecting material degradation during several cycles.

The PEDOT:PSS-based electrode (Fig. S7c) shows the formation of the SEI in the first cycle, but the voltage drop is less sharp than in the WO_3 or PPy samples. This suggests that PEDOT forms a more stable SEI layer with less capacity loss during the first cycle.

By the 30th cycle, PEDOT:PSS maintains its status as the most stable material. The charge and discharge curves remain close together, with little capacity loss. This demonstrates that PEDOT has the best capacity retention among the tested materials, making it ideal for long-term cycling applications.

The PANi-based electrode (Fig. S7d) shows the typical SEI formation behavior in the first discharge cycle, similar to the other materials.

In the 30th cycle, PANi shows significant capacity loss, with a significant variation in the charge-discharge curves. Although it outperforms WO_3, its stability is inferior to PEDOT:PSS electrode, indicating that PANi is more disposed to degradation over extended

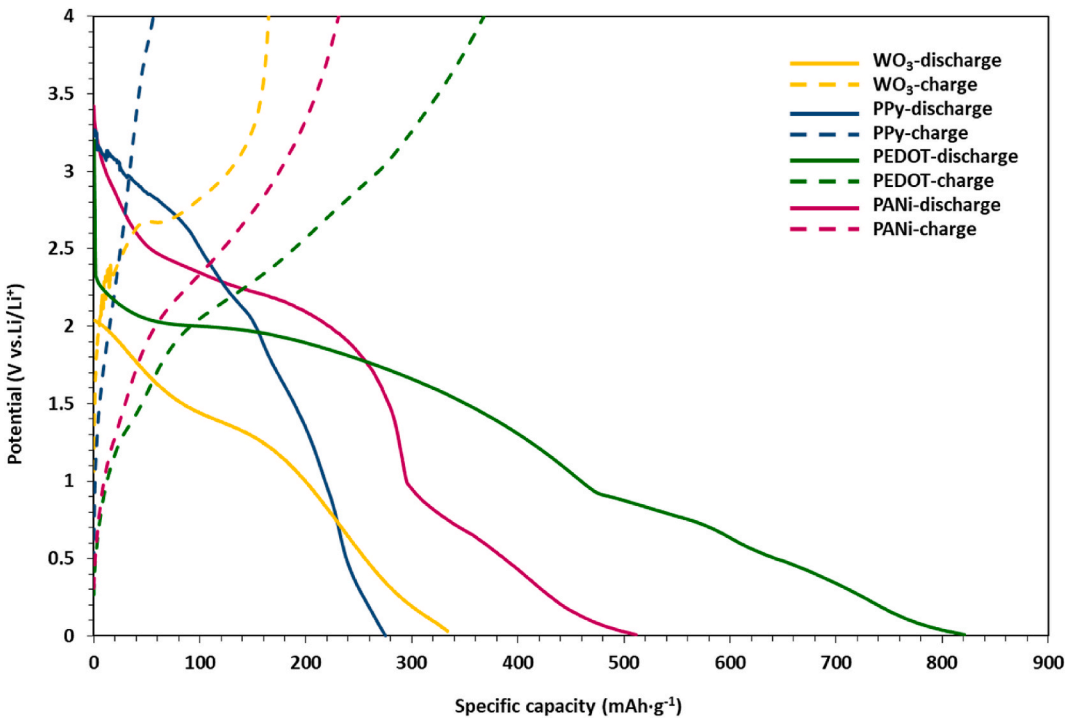

Fig. 10. Charge/discharge curves of WO_3, PPy coating, PEDOT coating and PANi coating.

cycling.

Capacity retention varying current density has been studied and it is shown in Fig. S8. The graph presents the specific capacity (mAh/g) of four different samples over 60 cycles, measured at various current densities (0.1, 0.5, 0.7, 1, and 2 A/g).

The PPy sample has the lowest initial specific capacity of approximately 200 mAh/g at 0.1 A/g. The capacity decreases significantly as the current density increases, with a marked drop at higher densities, particularly at 2 A/g. Finally, there is a capacity recovery when the current density returns to 0.1 A/g, but the recovery is minimal, stabilizing around 150 mAh/g.

In case of PEDOT:PSS electrode, it demonstrates the highest specific capacity among all samples, starting at around 800 mAh/g at 0.1 A/g. There is a gradual decrease in specific capacity as the current density increases to 0.5, 0.7, 1, and 2 A/g, indicating a typical trend of capacity fading with higher current densities. Interestingly, after the current density returns to 0.1 A/g around cycle 50, the specific capacity partially recovers, reaching close to 700 mAh/g. This suggests that the material is capable of recovering some of its capacity when the current density is reduced.

So, the specific capacity of all samples decreases with increasing current density, which is expected due to the faster charge/discharge rates and the increased internal resistance. Among the samples, the PEDOT:PSS electrode shows the best performance in terms of maintaining a high specific capacity and recovering capacity after high current density cycling.

The PANi and WO3 samples exhibit moderate performance, with some capacity recovery after high current density, though they suffer from more pronounced capacity fading.

However, the PPy sample shows the lowest capacity and the least recovery, indicating that it might be less suitable for high-power applications."

The bar graph shown in Fig. S9 represents the specific capacity retention of each electrode after 30 charge-discharge cycles. In other words, it shows how much of the original specific capacity the electrode still has after undergoing 30 cycles of use.

The WO_3 electrode retains a significant portion of its original specific capacity after 30 cycles, suggesting decent stability. However, it does not perform as well as the PEDOT:PSS electrode but performs better than the PANi sample.

PPy electrode has the lowest capacity retention, indicating that it has lost a large portion of its specific capacity after 30 cycles. This suggests poor cycling stability or a higher degree of degradation over time [46,47].

Fig. S9 clearly shows that PEDOT:PSS has the highest retention of specific capacity, meaning it suffers the least degradation after 30 cycles, making it a more suitable candidate for applications requiring long-term cycling stability. In contrast, PPy electrode loses the most capacity, indicating poor cycling stability.

3.5.3. EIS characterization

To comprehensively investigate the electrochemical performance of each electrode, Electrochemical Impedance Spectroscopy (EIS) was conducted on WO_3, PPy-WO_3, PEDOT:PSS-WO_3, and PANi-WO_3 samples. These analyses were performed both prior to cycling and

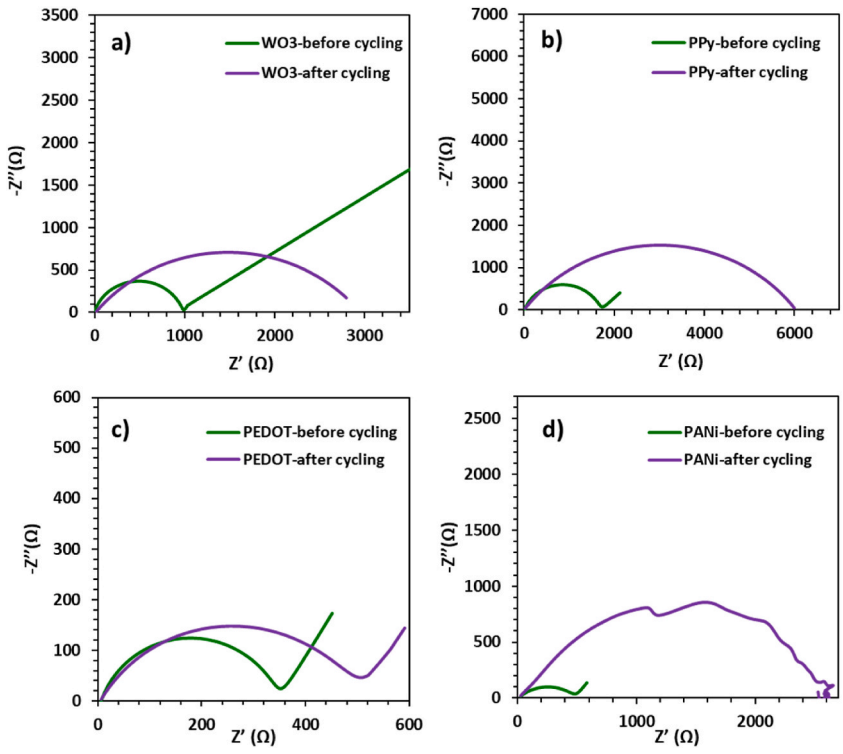

Fig. 11. Nyquist plots before and after the cycling of nanostructures based on a) WO_3, b) PPy coating, c) PEDOT coating and d) PANI coating.

after 30 charge/discharge cycles, spanning a frequency range from 10^4 to 0.01 Hz. As observed in the Nyquist plots (Fig. 11), the spectra obtained before cycling exhibit a semicircle at high and medium frequencies, while a sloping line is evident at lower frequencies. These spectra have been adjusted according to the equivalent circuits shown in Fig. S10. The spectra obtained before the charging and discharging cycles (shown in green in Fig. 11) were adjusted according to the equivalent circuit of Figure S10 a, while the spectra obtained after the 30 charging and discharging cycles (shown in violet in Fig. 11) were adjusted according to the equivalent circuit shown in Figure S10 b, with the exception of the electrode polymerized with PEDOT:PSS. The latter was also fitted according to the circuit in Figure S4 a since it showed the inclined line referring to the presence of Warburg, as mentioned above.

In addition, the results concerning the resistances obtained in this characterization after the adjustment according to the models presented in Fig. S10 are shown in Table S3.

Before cycling, the spectra display a semicircle at high and medium frequencies, accompanied by a line exhibiting a 45-degree slope at low frequencies. However, these spectra change after the cycles of charge and discharge, as observed in Fig. 11, where the width of the semicircle increases, indicating higher resistance to the transfer of ions from the electrolyte responsible for providing good specific charge and discharge capacity. Additionally, the line with slope disappears in electrodes without the polymer layer, as well as in electrodes with the PPy coating, confirming the previously obtained results where their electrochemical properties were inferior.

As discussed in section 3.4, when the semicircle intersects the x-axis at high frequencies (denoted as Z′) the cutoff value is obtained, which is linked to the sum of the Rs and Rp, where Rs is linked to the resistance of the electrolyte and Rp to the resistance that the polymer may oppose to the diffusion process. The extent of the semicircle reflects the charge transfer resistance (Rct), while the constant phase element represents the electrical capacitance of the double-layer at the electrode/electrolyte interface. Furthermore, the inclined line observed in the low-frequency region (denoted as Zw) is associated with Warburg behavior, which is indicative of the Li-ion diffusion process, as suggested by previous research [4,48].

The combined ohmic resistances (Rs + Rp) exhibit minimal variation among all samples, indicating that all electrodes demonstrate comparable conductivity upon contact with the electrolyte. Notably, the width of the electrode semicircle with a PEDOT:PSS coating is much smaller than the rest of the electrodes, indicating lower resistance to charge transfer and thus favoring the energy storage [49]. Additionally, in this case, both before and after cycling, the Warburg component appears, indicating that ion diffusion is not hindered, and it continues to be produced charging and discharging processes. Finally, the difference in the width of the semicircle before and after cycling is much smaller in this case, indicating that this coating protects the nanostructures, preventing a significant increase in charge transfer resistance.

These results are reliable with all those observed in the previous characterizations, and therefore, it can be affirmed that the electrode synthesized with WO_3 and coated with PEDOT:PSS exhibits the best properties and demonstrates superior electrochemical behavior.

In Fig. S11 the Randles plot is presented, which is commonly used to analyze electrochemical impedance data and determine the diffusion coefficients of ions in different electrode materials. The x-axis represents the square root of the inverse angular frequency (ω-1/2 in Hz-1/2), while the y-axis shows the real component of impedance (Re Z′) in ohms (Ω).

The diffusion coefficients are inversely proportional to the impedance values in the Randles plot. Materials with lower impedance typically allow for faster ion diffusion. However, the differences in diffusion coefficients between the electrodes are minimal, as indicated by the similarity of the curves for the polymer-based electrodes.

To calculate the diffusion coefficient (D) from the Randles plot, we use the slope of the linear portion of the graph and apply the following equation:

$$k_w = \frac{R \cdot T}{n^2 \cdot F^2 \cdot A\sqrt{2}} \cdot \left(\frac{1}{D^{1/2} \cdot C^*}\right)$$

In which kw is the slope from the Randles circuit, T is the temperature value (K), R corresponds to the gas constant, F is the Faraday constant, n is related to the charge transfer number, A is associated with the area of the electrode surface, C* is ionic concentration and D is the diffusion coefficient.

Table S4 shows the diffusion coefficient obtained, which aligns with values reported in the literature for WO_3 [50,51]. Furthermore, it indicates that the ion diffusion is primarily governed by the action of WO_3. The polymer coatings (PEDOT, PPy, and PANi) do not significantly interfere with the ion diffusion process, as evidenced by the minimal differences in impedance values between them. PEDOT exhibits a slightly higher diffusion resistance, but this difference is not substantial enough to suggest a major impact on ion transport. Therefore, the overall ion diffusion behavior is largely determined by the WO_3 material.

4. Conclusions

To sum up, a simplistic and low-cost electrochemical method is used for the synthesis of WO_3 nanostructres and deposition of different polymer coatings on them. After morphological and topographic characterization, it has been verified that nanostructures coated with PEDOT:PSS polymer exhibit greater roughness and improved wettability. This results enhanced the accessibility of the electrolyte used in Li-ion batteries to the entire electrode, providing a larger available active area.

Furthermore, electrochemical characterization has demonstrated that this coating exhibits lower resistance associated to charge transfer and a greater electrochemically active area (ECSA), as evidenced by double-layer capacitance tests.

Finally, electrodes from each polymer that exhibited the best properties in the previous characterizations were tested in Li-ion batteries application. Once again, it was determined that PEDOT:PSS polymer offers higher specific capacity in the charging and

discharging processes of lithium-ion batteries (817 mA h g^{-1}), specifically 2.5 times higher compared to the basic WO_3 electrode. Moreover, employing Electrochemical Impedance Spectroscopy (EIS) on the batteries both before and after cycling revealed that the PEDOT:PSS coating provides greater electrode protection, preventing rapid deterioration of its properties and consequently extending its lifespan.

CRediT authorship contribution statement

Gemma Roselló-Márquez: Writing – original draft, Visualization, Software, Resources, Methodology, Investigation, Formal analysis, Data curation, Conceptualization. **Dionisio Miguel García-García:** Writing – review & editing, Validation, Supervision. **Mireia Cifre-Herrando:** Writing – review & editing, Methodology. **José García-Antón:** Writing – review & editing, Validation, Investigation, Funding acquisition.

Data availability statement

Data Available on request.

Declaration of competing interest

The authors declare that they have no known competing financial interests or personal relationships that could have appeared to influence the work reported in this paper.

Acknowledgments

The authors wish to thank the economic support granted by AEI (PID2019-105844RB-I00/AEI/10.13039/501100011033). G. Roselló-Márquez is also grateful to UPV for the post-doctoral grant (PAID-10-21) and the grant to support postdoctoral research at UPV (PAID-PD-22), as well as to Generalitat Valenciana for the research stays in centers located outside the Valencian Community (CIBEST 2022). M. Cifre-Herrando acknowledges the Ministerio de Universidades for the pre-doctoral grant (FPU19/02466).

Appendix A. Supplementary data

Supplementary data to this article can be found online at https://doi.org/10.1016/j.heliyon.2024.e41075.

References

[1] C. Dulgerbaki, N. Nohut Maslakci, A.I. Komur, A. Uygun Oksuz, PEDOT/WO3 hybrid nanofiber architectures for high performance electrochromic devices, Electroanalysis 28 (2016) 1873–1879, https://doi.org/10.1002/elan.201501154.
[2] X. Fan, B. Gao, T. Wang, X. Huang, H. Gong, H. Xue, H. Guo, L. Song, W. Xia, J. He, Layered double hydroxide modified WO3 nanorod arrays for enhanced photoelectrochemical water splitting, Appl. Catal. Gen. 528 (2016) 52–58, https://doi.org/10.1016/j.apcata.2016.09.014.
[3] Y. Huang, Y. Li, G. Zhang, W. Liu, D. Li, R. Chen, F. Zheng, H. Ni, Simple synthesis of 1D, 2D and 3D WO3 nanostructures on stainless steel substrate for high-performance supercapacitors, J. Alloys Compd. 778 (2019) 603–611, https://doi.org/10.1016/j.jallcom.2018.11.212.
[4] F. Wang, X. Zhan, Z. Cheng, Z. Wang, Q. Wang, K. Xu, M. Safdar, J. He, Tungsten oxide@polypyrrole core-shell nanowire arrays as novel negative electrodes for asymmetric supercapacitors, Small 11 (2015) 749–755, https://doi.org/10.1002/smll.201402340.
[5] A.O. Efremova, E.G. Tolstopjatova, R. Holze, V.V. Kondratiev, Interactions in electrodeposited poly-3,4-ethylenedioxythiophene—tungsten oxide composite films studied with spectroelectrochemistry, Polymers 13 (2021), https://doi.org/10.3390/polym13101630.
[6] C. Janáky, N.R. De Tacconi, W. Chanmanee, K. Rajeshwar, Bringing conjugated polymers and oxide nanoarchitectures into intimate contact: light-induced electrodeposition of polypyrrole and polyaniline on nanoporous WO 3 or TiO 2 nanotube array, J. Phys. Chem. C 116 (2012) 19145–19155, https://doi.org/10.1021/jp305181h.
[7] Y. Shi, Y. Zhang, K. Tang, J. Cui, X. Shu, Y. Wang, J. Liu, Y. Jiang, H.H. Tan, Y. Wu, Designed growth of WO3/PEDOT core/shell hybrid nanorod arrays with modulated electrochromic properties, Chem. Eng. J. 355 (2019) 942–951, https://doi.org/10.1016/j.cej.2018.08.163.
[8] M.K. Zadeh, M. Yeganeh, M.T. Shoushtari, A. Esmaeilkhanian, Corrosion performance of polypyrrole-coated metals: a review of perspectives and recent advances, Synth. Met. 274 (2021) 116723, https://doi.org/10.1016/j.synthmet.2021.116723.
[9] Y. Jia, P. Xiao, H. He, J. Yao, F. Liu, Z. Wang, Y. Li, Photoelectrochemical properties of polypyrrole/TiO 2 nanotube arrays nanocomposite under visible light, Appl. Surf. Sci. 258 (2012) 6627–6631, https://doi.org/10.1016/j.apsusc.2012.03.092.
[10] D.V. Zhuzhelskii, E.G. Tolstopjatova, S.N. Eliseeva, A.V. Ivanov, S. Miao, V.V. Kondratiev, Electrochemical properties of PEDOT/WO 3 composite films for high performance supercapacitor application, Electrochim. Acta 299 (2019) 182–190, https://doi.org/10.1016/j.electacta.2019.01.007.
[11] G. Roselló-Márquez, D.M. García-García, M. Cifre-Herrando, E. Blasco-Tamarit, J. García-Antón, Facile preparation of electrodes based on WO3 nanostructures modified with C and S used as anode materials for Li-ion batteries, J. Am. Ceram. Soc. 106 (2023) 2550–2566, https://doi.org/10.1111/jace.18910.
[12] M.A. Chougule, S.G. Pawar, P.R. Godse, R.N. Mulik, S. Sen, V.B. Patil, Synthesis and characterization of polypyrrole (PPy) thin films, Soft Nanoscience Letters 01 (2011) 6–10, https://doi.org/10.4236/snl.2011.11002.
[13] D.M. Morales, M. Risch, Seven steps to reliable cyclic voltammetry measurements for the determination of double layer capacitance, JPhys Energy 3 (2021), https://doi.org/10.1088/2515-7655/abee33.
[14] M. Sasidharan, N. Gunawardhana, M. Yoshio, K. Nakashima, WO 3 hollow nanospheres for high-lithium storage capacity and good cyclability, Nano Energy 1 (2012) 503–508, https://doi.org/10.1016/j.nanoen.2012.03.003.
[15] F. Wolfart, D.P. Dubal, M. Vidotti, R. Holze, P. Gómez-Romero, Electrochemical supercapacitive properties of polypyrrole thin films: influence of the electropolymerization methods, J. Solid State Electrochem. 20 (2016) 901–910, https://doi.org/10.1007/s10008-015-2960-2.

[16] M. Beygisangchin, S.A. Rashid, S. Shafie, A.R. Sadrolhosseini, H.N. Lim, Preparations, properties, and applications of polyaniline and polyaniline thin films—a review, Polymers 13 (2021), https://doi.org/10.3390/polym13122003.

[17] M. Getnet Tadesse, C. Loghin, Y. Chen, L. Wang, D. Catalin, V. Nierstrasz, Effect of liquid immersion of PEDOT: PSS-coated polyester fabric on surface resistance and wettability, Smart Mater. Struct. 26 (2017), https://doi.org/10.1088/1361-665X/aa6f25.

[18] B.A. Mei, O. Munteshari, J. Lau, B. Dunn, L. Pilon, Physical interpretations of nyquist plots for EDLC electrodes and devices, J. Phys. Chem. C 122 (2018) 194–206, https://doi.org/10.1021/acs.jpcc.7b10582.

[19] A. Azioune, M.M. Chehimi, B. Miksa, T. Basinska, S. Slomkowski, Hydrophobic protein-polypyrrole interactions: The role of van der Waals and Lewis acid-base forces as determined by contact angle measurements, Langmuir 18 (2002) 1150–1156, https://doi.org/10.1021/la010444o.

[20] F. Wang, F. Varenne, D. Ortiz, V. Pinzio, M. Mostafavi, S. Le Caër, Degradation of an ethylene carbonate/diethyl carbonate mixture by using ionizing radiation, ChemPhysChem 18 (2017) 2799–2806, https://doi.org/10.1002/cphc.201700320.

[21] C. Duc, A. Vlandas, G.G. Malliaras, V. Senez, Wettability of PEDOT:PSS films, Soft Matter 12 (2016) 5146–5153, https://doi.org/10.1039/c6sm00599c.

[22] M. Guzinski, J.M. Jarvis, F. Perez, B.D. Pendley, E. Lindner, R. De Marco, G.A. Crespo, R.G. Acres, R. Walker, J. Bishop, PEDOT(PSS) as solid contact for ion-selective electrodes: the influence of the PEDOT(PSS) film thickness on the equilibration times, Anal. Chem. 89 (2017) 3508–3516, https://doi.org/10.1021/acs.analchem.6b04625.

[23] Z. Zhang, Z. Wei, M. Wan, Nanostructures of polyaniline doped with inorganic acids, Macromolecules 35 (2002) 5937–5942, https://doi.org/10.1021/ma020199v.

[24] J. Tan, Z. Zhang, Y. He, Q. Yue, Z. Xie, H. Ji, Y. Sun, W. Shi, D. Ge, Electrochemical synthesis of conductive, superhydrophobic and adhesive polypyrrole-polydopamine nanowires, Synth. Met. 234 (2017) 86–94, https://doi.org/10.1016/j.synthmet.2017.10.012.

[25] E.N. Konyushenko, J. Stejskal, M. Trchová, J. Hradil, J. Kovářová, J. Prokeš, M. Cieslar, J.Y. Hwang, K.H. Chen, I. Sapurina, Multi-wall carbon nanotubes coated with polyaniline, Polymer (Guildf) 47 (2006) 5715–5723, https://doi.org/10.1016/j.polymer.2006.05.059.

[26] C.H. Srinivas, Synthesis and characterization of nano size conducting polyaniline, IOSR J. Appl. Phys. 1 (2012) 12–15, https://doi.org/10.9790/4861-0151215.

[27] B. Kavitha, K. Siva Kumar, N. Narsimlu, Synthesis and characterization of polyaniline nano-fibers, Indian J. Pure Appl. Phys. 51 (2013) 207–209.

[28] A. Olad, B. Naseri, Preparation, characterization and anticorrosive properties of a novel polyaniline/clinoptilolite nanocomposite, Prog Org Coat 67 (2010) 233–238, https://doi.org/10.1016/j.porgcoat.2009.12.003.

[29] S. Sathiyanarayanan, S. Syed Azim, G. Venkatachari, Preparation of polyaniline-TiO2 composite and its comparative corrosion protection performance with polyaniline, Synth. Met. 157 (2007) 205–213, https://doi.org/10.1016/j.synthmet.2007.01.012.

[30] V.S. Jamadade, D.S. Dhawale, C.D. Lokhande, Studies on electrosynthesized leucoemeraldine, emeraldine and pernigraniline forms of polyaniline films and their supercapacitive behavior, Synth. Met. 160 (2010) 955–960, https://doi.org/10.1016/j.synthmet.2010.02.007.

[31] J. Kim, C. Park, S. Im, H. Lee, J.H. Kim, Effect of molecular weight distribution of PSSA on electrical conductivity of PEDOT:PSS, RSC Adv. 9 (2019) 4028–4034, https://doi.org/10.1039/c8ra09919g.

[32] B.A. Mei, J. Lau, T. Lin, S.H. Tolbert, B.S. Dunn, L. Pilon, Physical interpretations of electrochemical impedance spectroscopy of redox active electrodes for electrical energy storage, J. Phys. Chem. C 122 (2018) 24499–24511, https://doi.org/10.1021/acs.jpcc.8b05241.

[33] H.D. Yoo, J.H. Jang, J.H. Ryu, Y. Park, S.M. Oh, Impedance analysis of porous carbon electrodes to predict rate capability of electric double-layer capacitors, J. Power Sources 267 (2014) 411–420, https://doi.org/10.1016/j.jpowsour.2014.05.058.

[34] K. Ma, C. Zhang, C.E. Woodward, X. Wang, Bridging the gap between macroscopic electrochemical measurements and microscopic molecular dynamic simulations: porous carbon supercapacitor with ionic liquids, Electrochim. Acta 289 (2018) 29–38, https://doi.org/10.1016/j.electacta.2018.09.016.

[35] V. Vivier, M.E. Orazem, Impedance analysis of electrochemical systems, Chem Rev 122 (2022) 11131–11168, https://doi.org/10.1021/acs.chemrev.1c00876.

[36] J. Huang, Z. Li, B.Y. Liaw, J. Zhang, Graphical analysis of electrochemical impedance spectroscopy data in Bode and Nyquist representations, J. Power Sources 309 (2016) 82–98, https://doi.org/10.1016/j.jpowsour.2016.01.073.

[37] J. Di, X. Gai, R. Jamakanga, J. Lou, M. Zhu, Y. Li, R. Yang, Q. Ma, Synthesis of 1D WO3 nanostructures using different capping agents for pseudocapacitor applications, J. Nanoparticle Res. 24 (2022), https://doi.org/10.1007/s11051-022-05604-2.

[38] B. Liu, Y. Wang, H.W. Jiang, B.X. Zou, WO3 nanowires on graphene sheets as negative electrode for supercapacitors, J. Nanomater. 2017 (2017), https://doi.org/10.1155/2017/2494109.

[39] F. Mashkoor, D. Kim, M. Zahid Ansari, A. Hakeem Anwer, M. Shoeb, C. Jeong, Synergistic effects of multifunctional nanostructured WO3-WS2 decorated on polypyrrole (WO3-WS2/PPy) for the removal of toxic heavy metals from wastewaters and high supercapacitor performance, J. Mol. Liq. 375 (2023) 121312, https://doi.org/10.1016/j.molliq.2023.121312.

[40] J. Sun, L. Liu, F. Yang, A WO3/PPy/ACF modified electrode in electrochemical system for simultaneous removal of heavy metal ion Cu2+ and organic acid, J. Hazard Mater. 394 (2020) 122534, https://doi.org/10.1016/j.jhazmat.2020.122534.

[41] S.P. Gupta, V.B. Patil, N.L. Tarwal, S.D. Bhame, S.W. Gosavi, I.S. Mulla, D.J. Late, S.S. Suryavanshi, P.S. Walke, Enhanced energy density and stability of self-assembled cauliflower of Pd doped monoclinic WO3 nanostructure supercapacitor, Mater. Chem. Phys. 225 (2019) 192–199, https://doi.org/10.1016/j.matchemphys.2018.12.077.

[42] R. Li, Y. Yang, H. Li, R. Fu, W. Tan, Y. Qin, Y. Tao, Y. Kong, Design and synthesis of tungsten trioxide/polypyrrole/graphene using attapulgite as template for high-performance supercapacitors, Electrochim. Acta 311 (2019) 123–131, https://doi.org/10.1016/j.electacta.2019.04.159.

[43] Y. Meng, J. Yin, L. Wang, X. Yang, X. Li, Y. Jiang, Facile WO3@PANI composite film for applications in double-layer photoelectrochromic supercapacitors, Mater. Lett. 335 (2023) 133809, https://doi.org/10.1016/j.matlet.2022.133809.

[44] S. Rudra, J. K, G. Thamizharasan, M. Pradhan, B. Rani, N.K. Sahu, A.K. Nayak, Fabrication of Mn3O4-WO3 nanoparticles based nanocomposites symmetric supercapacitor device for enhanced energy storage performance under neutral electrolyte, Electrochim. Acta 406 (2022) 139870, https://doi.org/10.1016/j.electacta.2022.139870.

[45] L. Ouyang, C. Musumeci, M.J. Jafari, T. Ederth, O. Inganäs, Imaging the phase separation between PEDOT and polyelectrolytes during processing of highly conductive PEDOT:PSS films, ACS Appl. Mater. Interfaces 7 (2015) 19764–19773, https://doi.org/10.1021/acsami.5b05439.

[46] R. Muruganantham, J.Y. Huang, P.J. Wu, L.Y. Kuo, C.C. Yang, Y.G. Lin, J. Li, W.R. Liu, Nano-crystalline Fe3V3O8 material as an efficient advanced anode for energy storage applications, J. Power Sources 613 (2024), https://doi.org/10.1016/j.jpowsour.2024.234947.

[47] R. Muruganantham, P.C. Chiang, W.R. Liu, Copper-diphosphide composites: a key factor evaluation and capacity enhancement route for high-energy lithium-ion storage, ACS Appl. Energy Mater. 1 (2018) 3674–3683, https://doi.org/10.1021/acsaem.8b00470.

[48] B. Hirschorn, M.E. Orazem, B. Tribollet, V. Vivier, I. Frateur, M. Musiani, Determination of effective capacitance and film thickness from constant-phase-element parameters, Electrochim. Acta 55 (2010) 6218–6227, https://doi.org/10.1016/j.electacta.2009.10.065.

[49] V. Cristino, S. Marinello, A. Molinari, S. Caramori, S. Carli, R. Boaretto, R. Argazzi, L. Meda, C.A. Bignozzi, Some aspects of the charge transfer dynamics in nanostructured WO3 films, J Mater Chem A Mater 4 (2016) 2995–3006, https://doi.org/10.1039/c5ta06887h.

[50] J. Kim, S. Choi, S. Kim, W. Liu, M. Wang, X. Diao, C.S. Lee, Surface morphology engineering of WO3 films for increasing Li ion insertion area in electrochromic supercapacitors (ECSCs), Electrochim. Acta 472 (2023), https://doi.org/10.1016/j.electacta.2023.143394.

[51] S.K. Park, H.J. Lee, M.H. Lee, H.S. Park, Hierarchically structured reduced graphene oxide/WO3 frameworks for an application into lithium ion battery anodes, Chem. Eng. J. 281 (2015) 724–729, https://doi.org/10.1016/j.cej.2015.07.009.